minerals

MDPI

Article

Hydrothermal Alteration of Etna Ash and Implications for Mars

Andrea Bloise [1,*], Chiara Benedetta Cannata [1,2,*] and Rosanna De Rosa [1]

[1] Department of Biology, Ecology and Earth Sciences, University of Calabria, Via Pietro Bucci, 87036 Rende (CS), Italy; derosa@unical.it

[2] E3 Soc. Coop. Startup, University of Calabria, 87036 Arcavacata di Rende (CS), Italy

* Correspondence: andrea.bloise@unical.it (A.B.); chiara.cannata@unical.it (C.B.C.)

Received: 3 May 2020; Accepted: 16 May 2020; Published: 17 May 2020



Abstract: Volcanic activity represents one of the main factors controlling the geological evolution of Mars, whose morphology has remarkable counterparts on Earth. Studies on the Martian surface revealed the widespread occurrences of newly formed minerals originated by the hydrothermal alteration of volcanic rocks. In this work, we carried out a series of experiments to test the reactions occurring during the hydrothermal alteration of basaltic ash from Etna (Italy) as a possible similar reaction fully grown on the Martian rock. The volcanic ash used for the hydrothermal alteration experiments was collected during the eruption of Etna in 2001, and its composition shares similarities with Martian bedrocks. Ash was altered under hydrothermal conditions at initial pH 5 at two temperatures (150 and 200 °C) and reaction times of 5, 10, and 31 days. After a number of runs, we attained analcime $NaAlSi_2O_6 \cdot H_2O$. Our findings are in line with the hypothesis that zeolite on Mars probably originated from a low-temperature hydrothermal environment. The conclusions accord with the assumption that the analcime crystals recognized on Mars formed under the same conditions as those of our experimental setups.

Keywords: Etna ash; hydrothermal alteration; analcime; Mars

1. Introduction

Previous studies on Martian rocks showed that the surface of Mars is mainly constituted of basaltic products and that processes controlling the modification of the surface during the geological past (Noachian period) are primarily water-related [1–15]. The alteration of the mineralogical composition of Mars rocks had been inferred from orbital observations, terrestrial analogs, local surface analyses by rovers' science payloads, and the study of Martian meteorites [16–21]. The discovery of hydrated minerals showed that hydrous reactions took place over the story of the planet [1–3] and that the mineralogical evolution of Martian's soil materials is controlled by the evolution of the weathering conditions. Chevrier and Mathe [22] report that the evolution of the Martian surface passed through three steps corresponding to the dominant weathering process acting in that period: (i) a clay-type weathering process characterized by a thick H_2O/CO_2-rich atmosphere (Noachian); (ii) a sulfate-type acidic weathering process when water became scarcer (Hesperian); (iii) very slow weathering by strongly oxidizing agents (H_2O_2, O_2) in cold and dry conditions (today). The secondary mineral assemblage in the most recently altered terrains (late Noachian–Hesperian) is dominated by sulfate and iron oxides, by contrast to the Earth which is characterized by carbonate, clays, and quartz sediments. The difference reflects the nature of the chemical factor promoting weathering: CO_2 for the Earth and likely SO_2 for Mars [23]. In older terrain, by contrast, clay minerals as well zeolites and ferric oxides have been identified in units dating from the Noachian period, when it is supposed that the basaltic rocks of the surface underwent to different alteration phenomena [1,3–5]. In particular,

hydrothermalism played a key role in the formation of zeolite outcrops of Mars [6–15]. Indeed, there is evidence of the presence of phyllosilicate and zeolite deposits on the planet [16–18], indicating the widespread aqueous alteration of the basaltic surface, some of which took place under hydrothermal conditions. Zeolite on Mars was discovered by OMEGA in Noachian terrains around Mawrth Vallis and Nili Fossae [18,24,25], Hellas basin [11,12], Eridania basin [13,15], Utopia Rupes [14], as well as in scattered outcrops in the southern highlands [1,25], often in association with impact craters [4,25]. Zeolites are hydrated aluminosilicate minerals made from interlinked tetrahedra of silica (SiO_4) andalumina (AlO_4). This structure is negatively charged and attracts the positive cations and water molecules sited inside the heart of the framework structure [26–29]. In the present study, we focused on the occurrence of analcime (zeolite), suspected in Noachian terrains. The analcime (zeolite) was identified by Compact Reconnaissance Imaging Spectrometer for Mars (CRISM) in craters to the north of the Hellas basin and to the west of Nile Fossae near the Antoniadi Basin [18,25]. Basaltic rocks have been identified in this locality by the analyses of the MGS-TES (Mars Global Surveyor Thermal Emission Spectrometer) [30–34]. Together with analcime, CRISM detected also a mineral assemblage composed of chlorite, hydrated silica, and Fe/Mg smectite. Considering that such a mineral assemblage is a product of hydrothermalism on Earth [35,36], it suggests that the hydrothermal circulation of fluids could represents their major formation process. Analcime is a sodium-rich zeolite ($NaAlSi_2O_6{\cdot}H_2O$) formed in hydrothermal conditions, as investigated on Massif Central in France and Icelandic basalts [37–39]. Analcime formations also occur in highly alkaline lake waters [40], as a result of weathering of tephra [41], and, infrequently, as a primary magmatic product [39,42,43]. During the past decade, experimental synthesis, aimed at the formation of zeolite on Mars, has received remarkable attention. In particular, basaltic glass was altered under temperatures higher than 150–200 °C, in the presence of CO_2 but allowing a pH > 7, and it was demonstrated that the formation of specific zeolites depends on the composition of the glass as well as on that of the hydrothermal solution [44–48].

In the present study, we focused on the occurrence of zeolites, suspected in Noachian terrains. We carried out a series of laboratory experiments to test the hydrothermal conditions able to reproduce the formation of analcime from terrestrial starting material, in order to infer the possible mechanisms and conditions at the origin of the zeolite minerals. We used as starting material ash from the 2001 Etna eruption [49,50], which shares similarities with Martian rocks. In particular, Etna ash falls in a field of basalts similar to Mars basalts from Gusev Crater and to some samples of Martian meteorites and Spirit Rover [51–53] (see also Section 3.1). In this context, and in the light of the potential implications for Mars, this work intends to evaluate how the experimental conditions can affect the growth of analcime in terms of morphology, size, and thermal stability. In nature, the observation of hydrothermal alterations shows the importance of the following factors: temperature, pH of the solutions, chemical composition, nature (crystalline or amorphous) of the starting material, and condition of the system (closed or opened).

The Etna ash was altered under hydrothermal conditions at initial pH = 5 at two different temperatures (*T*: 150 and 200 °C) with run time (t) ranging between 5 and 31 days. These experimental conditions were adopted taking into account that: (i) relatively low-temperature hydrothermalism (<350 °C) is assumed to have played a key role in the formation of the zeolite outcrops of Mars [5]; (ii) the interaction of water and volcanic glass at low temperatures (usually <250 °C) readily yields zeolite minerals [54]; (iii) subcritical solvothermal synthesis (usually operating from 150 to 250 °C) has been well demonstrated by the successful synthesis of zeolites [6]; (iv) laboratory and theoretical studies demonstrate that acidic aqueous solutions played an important role in the dissolution of basaltic ashes on Mars [22,23,55–57]. The water reactant is assumed to be moderately acid (pH = 5), since an acidic environment during the early Noachian Period is presumed [7,22]. It derived from the oxidation and dissolution of volcanically produced acid gas in pure water [57]. An additional aspect to be taken into account is that the atmosphere's composition in which weathering develops has an influence on the nature of the secondary phases. Indeed, the atmosphere can affect the pH of the hydrosphere. Previous studies have shown that the chemical composition of the Martian atmosphere,

which is rich in CO_2 (95%), at adequate pressure influences the pH of solutions at equilibrium [58]. Thus, CO_2/SO_2-rich atmospheres were equilibrated with acid solutions.

2. Materials and Methods

2.1. Analysis of Ash and Mineral Phases

The starting material (ash) was first observed under an optical microscope (OM) (20x, 116 ZEISS, Thornwood, NY, USA) in order to characterize the components of the ash and their morphology. Successively, X-ray fluorescence (XRF) and X-ray powder diffraction (XRPD) analyses were made to determine the main mineral phases and the whole composition of major and minor elements of the ash. Transmission and scanning electron microscopy (TEM and SEM) coupled with EDS electron microprobes for chemical analysis, derivative thermogravimetry (DTG), and differential scanning calorimetry (DSC) analyses were conducted for a more detailed definition of the morphology, size, and chemical composition of the individual phases. XRPD patterns were obtained by a Bruker D8Advance (Bruker, Billerica, MA, USA) X-ray diffractometer with CuKa radiation, monochromated with a graphite sample, operating at 40 mA and 40 kV. Scans were collected in the range of 3–66° (2θ), with a step-counting time of 3 s and a step interval of 0.02°. DIFFRACplus EVA software (version 11.0., Bruker, Karlsruhe, Germany) was used to identify the mineral phases. An assessment of the mineralogical and amorphous phases present in the ash was attain by Rietveld refinements [59,60], tooled using TOPAS software V.4.2 (Bruker, Karlsruhe, Germany). XRF was used to determine the chemical composition of the ash, in terms of the major and minor elements (SiO_2, Na_2O, K_2O, Fe_2O_3, MnO, Al_2O_3, MgO, CaO, P_2O_5, and TiO_2), by using a Bruker S8 Tiger WD X-ray fluorescence spectrometer (Bruker, Karlsruhe, Germany), with a rhodium tube (XRF beam of 34 mm and intensity 4 kW). The analysis was carried out using 6 g of specimen, on pressed powder pellets placed over boric acid (maximum working pressure 25 bar). Secondary electron SEM imaging was carried out using the Field-Emission Scanning Electron Microscope FEI QUANTA 200 (Thermo Fisher Scientific, 120 Waltham, MA, USA), equipped with an X-ray EDS suite comprising a Si/Li crystal detector, model EDAX-GENESIS 4000 (EDAX Inc., Mahwah, NJ, USA). Detector constants and work conditions were as follows: tilt angle 0° and voltage 20 kV. Thermal analysis was carried out by Netzsch STA 449 C Jupiter (DSC/TGA: Netzsch STA 449 C Jupiter, Netzsch-Gerätebau GmbH, Selb, Germany). Heating was carried out in alumina crucibles at a heating rate of 10 °C/min under an air flow of 30 $cm^3 \cdot min^{-1}$. Samples were ground in an agate mortar, and about 10 mg was heated to a temperature in the range of 25–600 °C. Thermal analysis accuracy was checked by six repeated collections using a kaolinite reference samples, revealing good theoretical weight sensitivity of 0.10 μg, DSC detection limit <1 μW, and reproducibility (instrumental T precision of ± 1.2 °C). Transmission electron microscopy (TEM) analysis was performed on a JEOL JEM 1400 Plus (120 kV) (Jeol, Tokyo, Japan), equipped with a Jeol large-area silicon drift detector SDD-EDS (Jeol, Tokyo, Japan) and a double tilt holder to obtain structural data using selected-area electron diffraction (SAED). Powdered samples were deposited on a copper mesh grid coated with 200 A carbon film. Contribution of each analysis carried out on the starting material and the experimental run products: (i) XRPD: identification, crystallinity, semi-quantitative abundance; (ii) SEM/EDS: morphology, chemical composition, identification of individual particles; (iii) TEM/EDS/SAED: morphology (at high magnifications), chemical composition, crystallinity of individual particles; (iv) DSC/DTG: thermal stability, identification.

2.2. Hydrothermal Alteration of Ashes

For the present study, hydrothermal alteration experiments were performed using the solvothermal method. This method has been already widely employed for the synthesis of zeolites [61]. Ash fragments were crushed using a Bleuler Rotary Mill (Sepor, Los Angeles, CA, USA) at a speed of 900 revolutions per min (rpm) for 3 s. In all experiments, 0.70 g of powder and 2–4 mL of H_2O (HCl was added to obtain pH = 5) were added into a Teflon-lined stainless-steel autoclave of 25 mL capacity. The hydrothermal

treatments of the ashes were carried out in a polytetrafluoroethylene (PTFE) lined autoclave, at two different temperatures, 150 °C and 200 °C, with an autogenous pressure [62,63] and reaction times of 5, 10, and 31 days; after heating, the autoclave was cooled to room temperature naturally. Subcritical solvothermal synthesis has been well demonstrated by the successful synthesis of zeolites. It is worth mentioning that hydrothermal processes correspond to the alteration of the host rock by aqueous fluids (>100 °C), generally induced by volcanic activity. Subcritical solvothermal synthesis utilizes temperatures below the critical point of water (374 °C) [63,64].

3. Results

3.1. Ashes Characterization

The volcanic ash used for the hydrothermal alteration experiments was collected during the eruption of Etna in 2001 [49,50]. In particular, ash samples were collected in between 18 July and 7 August, when explosive activity occurred in the form of fire fountaining, strombolian explosions, hydromagmatic explosions, and pulsing ash explosions [49]. It is worth remembering that the ashes were not altered by atmospheric agents or anything else, before being hydrothermally altered in the laboratory. Under the OM (Figure 1), the ash appeared to consist of single crystals, tachylyte, and sideromelane glass fragments.

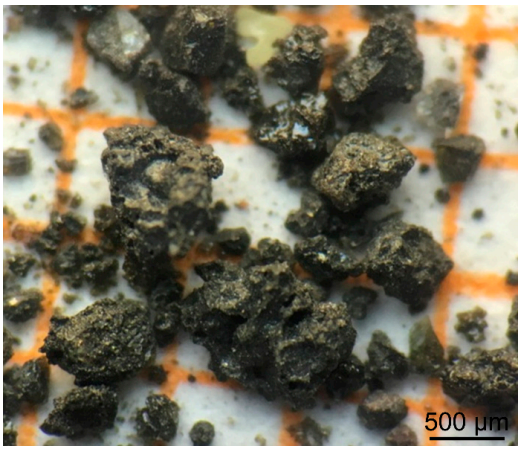


Figure 1. Optical image of ash from the 2001 Etna eruption.

Under SEM, the sideromelane appeared highly vesiculated, with round bubbles (Figure 2a), while the tachylite fragments (Figure 2b) were bubbles-poor, with blocky shapes.

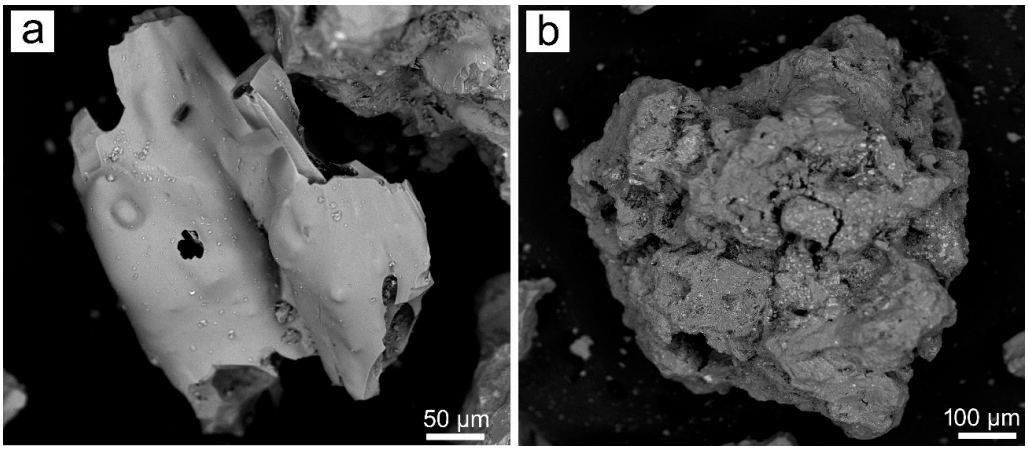


Figure 2. SEM images of sideromelane (**a**) and tachylite (**b**) glass fragments.

XRPD pointed out that the volcanic ash consists of plagioclase (44%), augite (39%), amorphous glass (10%), and olivine (7%), in a decreasing order of abundance (Figure 3). XRF analyses revealed that the ash is basaltic, with 46.7 wt.% of SiO_2 and 4.66 wt.% of Na_2O + K_2O (Table 1).

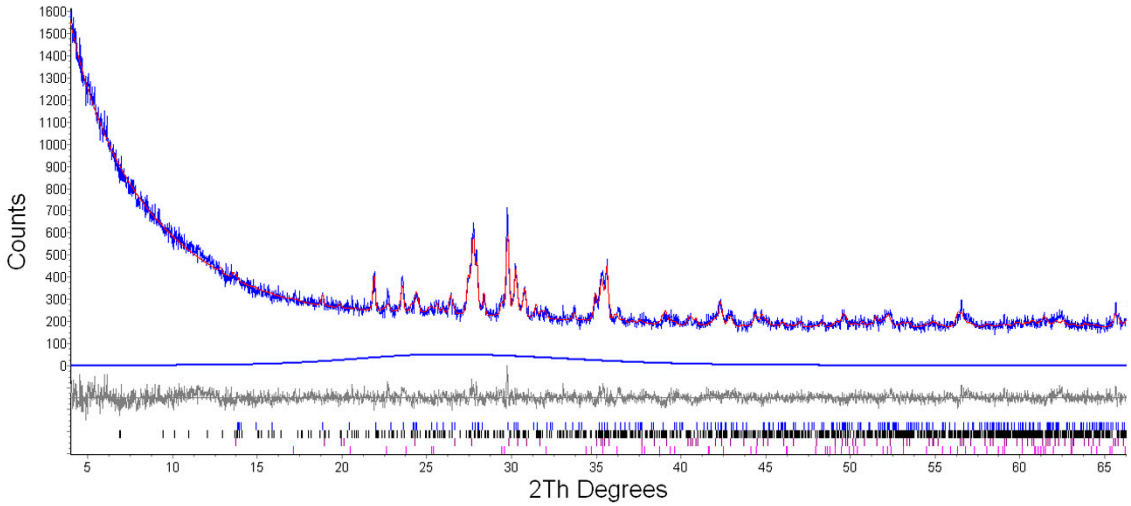


Figure 3. View (3–66° 2θ) of the Rietveld plots of the ash data collected. The blue curve (below) represents the glass. The grey curve represents the difference between observed and calculated plots. Vertical bars mark the position of calculated Bragg reflections of (from top to bottom) plagioclase (albite, anorthite), pyroxene (augite), and olivine.

Table 1. Chemical composition of major and minor elements of Etna ash (volcano eruption 2001) by XRF analysis (wt.%). L.O.I = loss on ignition.

Oxides	SiO_2	Na_2O	K_2O	Fe_2O_3	FeO	MnO	Al_2O_3	MgO	CaO	P_2O_5	TiO_2	L.O.I.
Wt.%	46.71	2.57	2.09	7.20	3.35	0.19	15.85	6.00	13.64	0.39	1.91	0.10

The chemical analysis of Etna ash is plotted on the binary TAS Alkali vs. Silica (Total Alkali vs. Silica) diagram; [65], which is a typical presentation for the classification of Earth igneous rocks [66]. In the same diagram (Figure 4), we plotted the chemistries of several Martian rocks acquired from orbital data and in situ [51,52]. In particular, we displayed the composition of the "Irvine" specimen, a mildly alkaline basalt discovered on the flanks of Columbia Hills (Gusev crater, Mars) obtained by the Alpha Particle X-ray Spectrometer (APXS; [53]) as well as an average of the chemical igneous composition of some samples of the Gale Crater Mars [67] obtained by the ChemCam Laser-Induced Breakdown Spectrometer (LIBS) in the MSL Curiosity rover. Moreover, the composition of the Martian meteorite Northwest Africa (NWA 6234) analyzed using the CAMECA SX-100 electron probe micro-analyzer, consistent with the composition of previously studied Martian meteorite basalts [68], was also reported in the TAS diagram (Figure 4). Etna ash (green square) fell in the field of basalts close to the Mars basalts from Gusev Crater (red triangle) and to some samples of Martian meteorites (grey full circles) and Spirit Rover (black full circles) (Figure 4). In this regard, basalt was chosen to depict the igneous rock type thought to cover some part of the Martian bedrock as ascertained from in situ XRF measurements of soils at the Viking landing sites [69] and from analysis of remotely sensed thermal emission data from Mars [30,70,71].

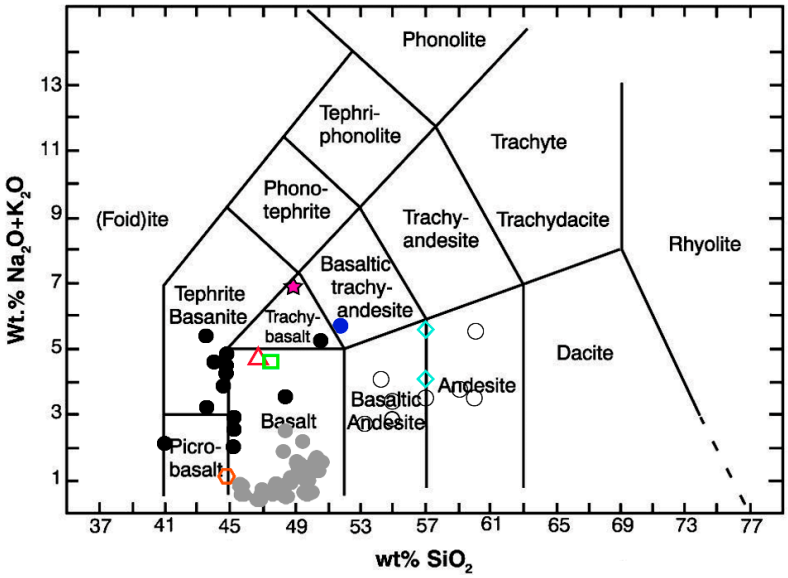


Figure 4. Total Alkalis vs. Silica (TAS) diagram of igneous rock, showing samples from Mars Gale Crater (blue circle • and pink star ★); Mars meteorites (grey full circles •); Spirit rover (black full circles •); Pathfinder (Blue diamond ◇); Mars Global Surveyor (black empty circles ◯); Gusev Crater (red triangle △); picro-basalt meteorite (orange polygon ⬠) in relation to the composition of ash from Etna eruption in 2001 (green square □).

3.2. Characterization of Run Products

3.2.1. XRPD

XRPD results showed that analcime was obtained during four runs, and a variable quantity of unreacted ash was also detected in all runs, including plagioclase $NaAlSi_3O_8$–$Ca(Al_2Si_2)O_8$, pyroxene $(Ca,Na)(Mg,Fe,Al)(Si,Al)_2O_6$, and olivine $(Mg,Fe)_2SiO_4$ (Figure 5). Ash did not react at 150 °C either after 5 or 10 days of hydrothermal alteration. Analcime $NaAlSi_2O_6{\cdot}H_2O$ started forming at 200 °C after 5 days of alterations (run Et3), when very tiny amounts of analcime crystals were obtained.

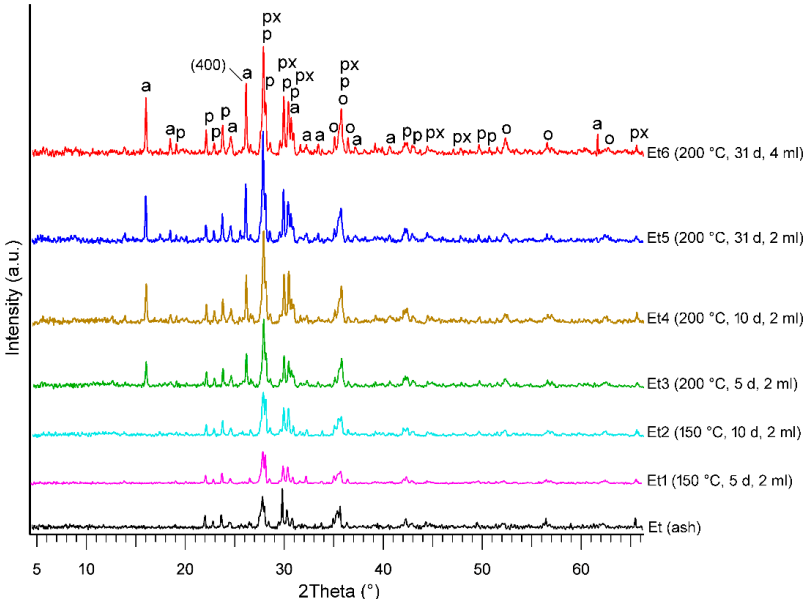


Figure 5. XRPD pattern from the starting material (Et) and products (Runs Et1–Et6). a = analcime; O = olivine; p = plagioclase; px = pyroxene. Peaks were assigned according to the literature.

At 200 °C, the increase of the reaction time from 5 to 10 days (run Et4) led to an increase in analcime production (Table 2). Under the same experimental conditions (T, water-to-rock ratio (W/R)), an increase in reaction time from 10 (run Et4) to 31 days (run Et5) enhanced the reactions towards a higher amount of analcime (Table 2). This result was inferred by the intensity (400) of analcime reflection at 8.060 (2θ) (Table 2); indeed, the reflection obtained from analcime synthesized in a shorter reaction (runs Et3, Et4) was lower in intensity, while a higher intensity was observed when analcime was formed in a longer reaction (run Et5).

Table 2. Experimental setup and list of the products obtained for each run in order of decreasing abundance, as detected by XRPD, TEM/EDS, and SEM/EDS. Full width at half-maximum (FWHM). P = plagioclase; Py = pyroxene; O = olivine; A = analcime. Et6 ash was altered with the addition of water from 2 mL to 4 mL. Water with initial pH = 5; water-to-rock ratio (W/R).

Runs	T (°C)	t (Days)	W (mL)	W/R (mL/g)	Mineral Abundance	Newly Formed Mineral	Analcime Peak Intensity (400) (cps)	Analcime FWHM (400) (Δ°2θ)
Et (ash)	-	-	-	-	P > Py > O	-	-	-
Et1	150	5	2	2.8	P > Py > O	-	-	-
Et2	150	10	2	2.8	P > Py > O	-	-	-
Et3	200	5	2	2.8	P > Py > O > An	An	353	0.154
Et4	200	10	2	2.8	P > Py > O > An	An	396	0.147
Et5	200	31	2	2.8	P > Py > O > An	An	459	0.147
Et6	200	31	4	5.7	P > Py > An > O	An	480	0.142

In run Et5, an increase in water from 2 mL to 4 mL at 200 °C (run Et6) improved the analcime yield. The results also showed that the sharpness of the main peak (400), which depicts the degree of crystallinity of analcime, increased with increasing reaction time and W/R. In particular, rising the reaction time from 5 to 31 days, under the same temperature of 200 °C (Et3–Et5), caused a decrease of the FWHM value from 0.154° to 0.147° (Table 2). A similar trend occurred when water was increased from 2 to 4 mL (Table 2), at 200 °C. Anyway, a complete reaction was not achieved, since unreacted starting materials (plagioclase, pyroxene, and olivine) were present in all runs. After the hydrothermal reaction, all the diagnostic reflections of the plagioclase, pyroxene and olivine were preserved (Figure 5).

3.2.2. SEM/TEM/EDS

In low-magnification images, the ash appeared to consist of different phases, both crystalline and amorphous, as verified by SAED, in agreement with the results of XRPD. As regards morphology, volcanic amorphous ash fragments showed low contrast in TEM images and a ring-shaped SAED pattern (Figure 6a). The amorphous ash particles were detected between the edges of the crystals (Figure 6a). The chemical composition of the glass is consistent with the elements being present in the stoichiometric composition of analcime (Si, Al, Na), in addition to the presence of low amounts of Fe and Ca. The most evident and abundant crystals corresponded to plagioclase, pyroxene, and olivine, characterized by well-defined edges and crystal size typically greater than 500 nm (Figure 6a). At 150 °C, the altered ash looked very similar to the untreated one, with apparently well-preserved morphology and size of the ash particles. However, at higher magnification, TEM investigations revealed that at 150 °C (run Et1, Et2), tiny variations on ash morphology occurred after both 5 and 10 days of alteration, and as a matter of fact, the ash contour started to be less defined and seemed to peel off in many layers (Figure 6b), although under SEM, no edge modifications could be detected in the runs Et1 and Et2. By increasing the time of hydrothermal synthesis, the alteration tended to become more evident under TEM.

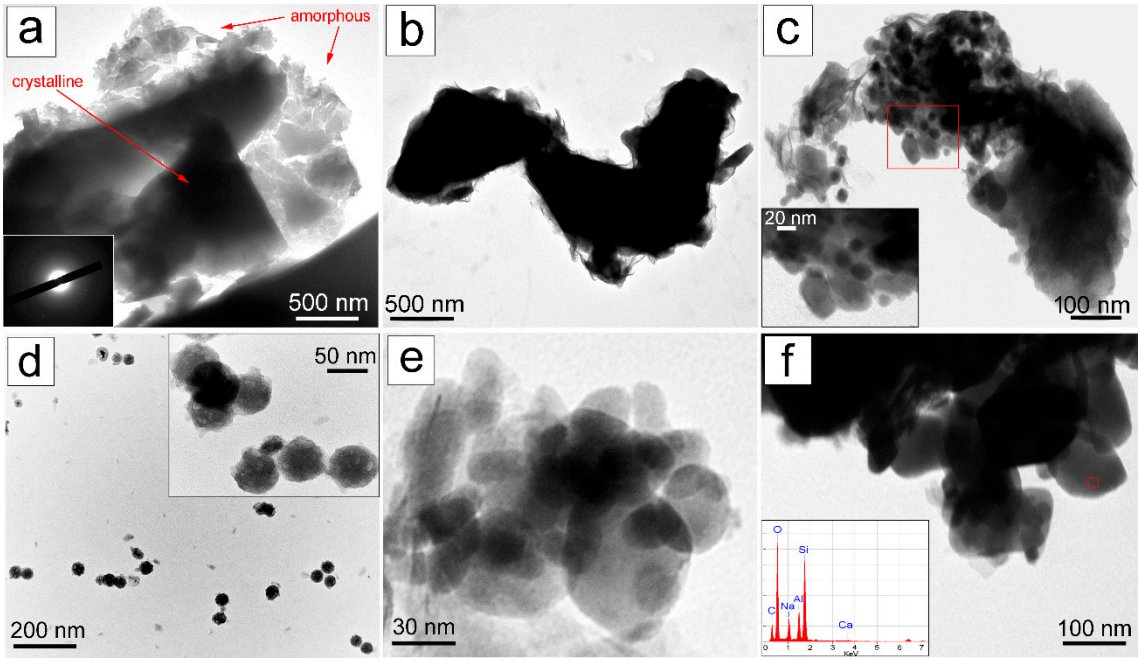


Figure 6. TEM micrograph of (**a**) ash Et, the inset shows the corresponding ring-shaped selected-area electron diffraction (SAED) pattern of the amorphous fragment; (**b**) run Et1; (**c**) analcime crystal (run Et3), magnification of the empty red rectangle showing aspheric analcime crystals; (**d**) analcime crystals (run Et4,) magnification of the empty black rectangle showing aspheric analcime crystals; (**e**) analcime crystals (run Et 5); (**f**) analcime crystals (run Et 6) with the relative EDS point analysis.

Ash contour began to completely fade after 5 days of alteration (run Et3), and the thickness of single fragments increasingly reduced, with the simultaneous appearance of spherical analcime crystals (Figure 6c). Under the same synthesis conditions (T, W/R), an increase in reaction time from 5 (run Et4) to 10 days (run Et4) improved the crystals size (Figure 6d). At 200 °C and reaction time of 31 days (run Et5), analcime crystallized into well-defined crystals (Figure 6e). TEM observations of Et3, Et4, and Et5 products testified a more intense alteration of the ash particles, whose dimensions and width tended to be progressively reduced. For the last run products (run Et6), the alteration engaged not only the amorphous ash contour but also the inner part of amorphous ash fragments. Indeed, a further increase in W/R (run Et6), led to an increase in analcime crystallinity, and newly formed euhedral analcime crystals were visible both under TEM and SEM (Figures 6f and 7). EDS/TEM qualitative chemical analysis showed that the composition of several analcime crystals from all runs consisted of Na, Al, O, and Si (Figure 6f). This result is in accordance with the idealized chemical formula of analcime: $NaAlSi_2O_6 \cdot H_2O$, although very a low amount of Ca was observed consisting of impurities derived from the starting materials (Figure 6f), as often also observed in natural samples [72]. The growth of analcime minerals on the top of the ash surface was further verified by SEM/EDS investigations (Figure 7a–c). Analcime assumed a cubic morphology [73,74], with size ranging from a few nm (Figure 7d,e) to some micrometer in width (Figure 7a–c). However, the SEM images showed that the analcime crystals were not equal in size and that unreacted phases (plagioclase, pyroxene, and olivine) were still present. The size of single crystals sometimes reached a maximum length of about 1.5 µm. As regards EDS/SEM chemical analysis, analcime was present in small crystals, often less than 1 µm in size, finely associated/covered with the starting materials (Figure 7). This prevented their pure EDS chemical characterization, leading to mixed analyses (analcime and unreacted phases). Another aspect to consider is that EDS micro-analysis is semi-quantitative, and the synthesized crystals should be polished in order to obtain an accurate evaluation; however, as shown in Figure 7, the crystals obtained in this study were too small to be polished.

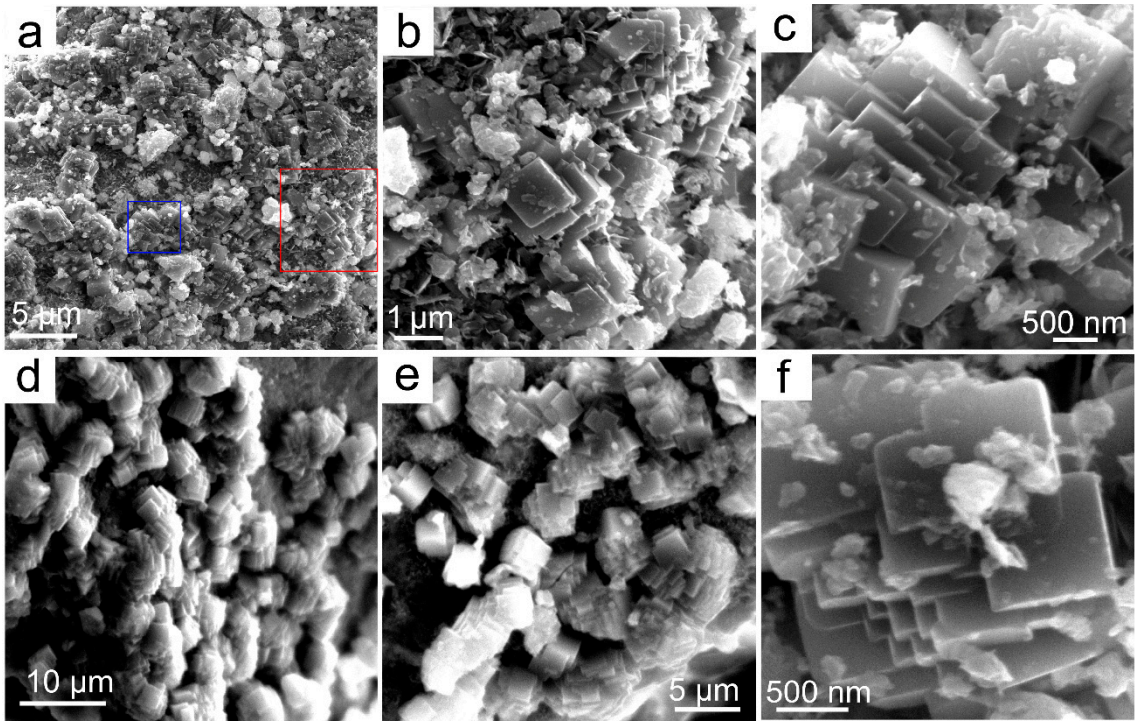


Figure 7. SEM micrograph of (**a**) analcime crystals synthesized in run Et5; (**b**) magnification of the area delimited by the red square in (a); (**c**) magnification of the area delimited by the blue square in micrograph (a); (**d**–**f**) analcime crystals synthesized in run Et6.

3.2.3. DSC/DTG Characterization

Analcime obtained in run Et6 was characterized by DSC/DTG to evaluate its thermal stability. Et6 was chosen being the run producing the highest amount of analcime.

The DSC curve of analcime exhibited one main endothermic peak at about 399 °C (Figure 8), linked to analcime breakdown, in agreement with literature data [75,76]. The endothermic peak can be related to the compensating cation–water binding energies. Analcime dehydrates between 350 °C and 450 °C, as shown in the DTG curve at about 399 °C. The DTG peak occurred as a consequence of the transfer of H_2O molecules through the six-member rings during dehydration [28,75]. The DSC peaks below 110 °C are related to the liberation of H_2O adsorbed on the samples' surface. Other phases (unreacted materials, i.e., pyroxene, plagioclase, and olivine) did not contribute to the thermal reaction, due to their high thermal stability [77].

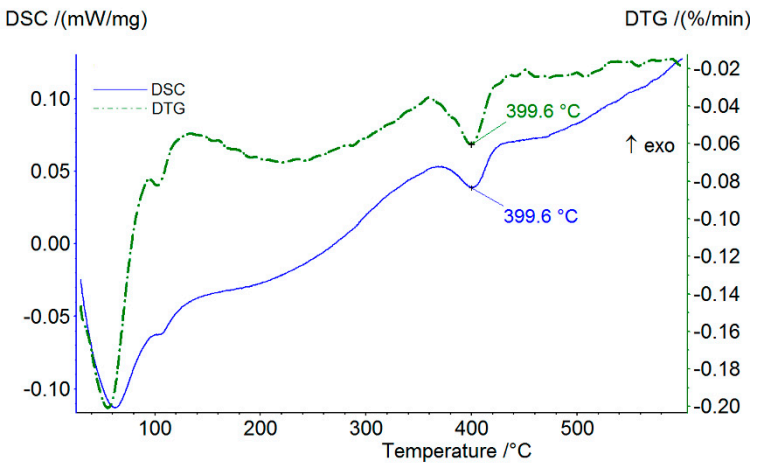


Figure 8. Thermal analysis of analcime from run Et6. Blue solid curve DSC; green dashed curve DTG.

4. Discussion and Conclusions

In this work, we provide a set of hydrothermal alteration experiments performed on basaltic ash presumably similar to Martian rocks, in order to mimic the physical condition for similar reactions on Mars. After a few runs, we obtained analcime. The results showed that the yield of analcime depended mainly on the temperature and the nature of the starting materials (i.e., amorphous and crystalline). In fact, as known, amorphous materials are more reactive than crystalline ones [77]. In this work, the amorphous material consisted of volcanic glasses of tachylite and sideromelane, which are considered products of relatively rapidly cooled magma, whose groundmass varies from a glassy and sub-aphyric texture to a micro- and/or crypto-crystalline one [49,78]. Ash pyroclasts, like tachylite and sideromelane, are subjected to physical and chemical alteration during syn-eruptive and post-eruptive processes. Our results revealed that analcime formed to the detriment of the amorphous material present in the ash, while silicate (plagioclase, pyroxene, and olivine) already occurring in the ash, did not take part in the hydrothermal reaction. As a matter of fact, during reactions at low T (150 °C), with reaction times corresponding to 5 and 10 days of alteration, the formation of analcime was inhibited, while at 200 °C analcime started to form.

As reported [79] for similar silicate syntheses, the increment of temperature induced higher SiO_2 reactivity, thus improving the reaction between the starting elements. Moreover, Berger et al. [80] showed that at a temperature of 475 °C, a supercritical CO_2–H_2O fluid led the recrystallization of a basalt glass in few days. Therefore, the solubility of silicate glass was confirmed to increase as the temperature rose from 150–200 °C to 475 °C, under hydrothermal conditions. These findings demonstrate how the chemical reactivity of usually insoluble starting materials can be hugely increased by increasing the temperature. The absence of a kinetic model for our experiment makes speculative the extrapolation of prediction of glass alteration over geological time [80,81]. However, it is not excluded that the low-temperature (150 °C) alteration of glass after hundreds of years could produce analcime as it occurs at 200 °C. The widespread occurrence of clay minerals discovered in Mars's Noachian terrains, indicating a long-duration interaction between water and rock [7], could support this hypothesis. The outcome confirmed that both fluid system (W/R > 1) and temperature (or reaction time) are essential for reaching a thorough amorphous glass alteration. The initial acidic pH likely promoted alkali leaching from the basaltic glass, and so the formation of secondary analcime, at least at high temperature. The final pH of the solution was not measured but is supposed to be alkaline, considering the low W/R ratio used in our experiments and as reported in previous literature on experimental studies on basalt glass alteration [81–83]. For example, Berger et al. [81] demonstrated that basalt glass alteration reached the steady state in solutions at pH 9.5, at which silica solubility increased, and the solution became enriched in both silica and alkali, promoting the precipitation of zeolite. In this context, we hypothesize that the leaching process preceding the glass network dissolution, promoted analcime formation.

Overall, in this work we point out that the highest yield of analcime occurred at 200 °C, with a reaction time of 31 days. Therefore, the experimental results are consistent with a low-temperature hydrothermal formation of analcime on Mars. These temperatures were very similar to those reported by Sætre et al. [44] for the synthesis of Ca-zeolite and lower amounts of analcime, wh used basaltic glass as a starting material.

The possible mechanisms by which analcime formed, such as circulations of fluids triggered by impact or by lava cooling, acid water/vapor, H_2O/CO_2-rich atmosphere, are currently absent on Mars. Today in fact, in dry atmosphere, the alteration is tenuous. As expected from its low dielectric constant, CO_2 does not interact with the silicate framework, and no secondary minerals originate. Indeed, in the present Martian environment, analcime may exist only as a metastable mineral. However, in the Noachian age, during which an H_2O/CO_2-rich hydrosphere/atmosphere was present, the formation of analcime could have been promoted by a low-temperature (<350 °C) hydrothermal fluid alteration of a basalt glass, primarily related to an impact crater setting or to lava cooling [5,7,14,18,25,45,84–87]. A modeled Martian impact inferred that hydrothermal systems give rise to circulating fluids and water

vapor [88,89] at temperature ranges that meet the conditions used in our experiments. We inferred also that a hydrothermal solution with acidic pH interacted with basaltic glass during the Noachian period, in agreement with literature data [7,22,90,91]. In particular, Wang et al. [86] indicated that a possible acidic environment (i.e., pH 4–6) in the past would have promoted the formation of kaolinite-type phyllosilicates, while Peretyazhko et al. [91] experimentally demonstrated that the weathering of a chemically representative Martian basaltic glass, with water at pH 4 under oxic atmosphere, led to the formation of Fe, Mg-smectites. In our experiments, the formation of Fe, Mg-phyllosilicates was inhibited in favor of that of zeolites formation. The nature of the secondary phase at low W/R, as in these experiments, is mainly constrained by temperature and pH, which in turn affect the Si/alkali ratio and product solubility, for zeolite at a temperature of 150–200 °C and final basic pH, for Fe, Mg-phyllosilicates at higher temperatures and acid pH [45]. In this regard, our research could shed new light on defining whether a part of the aqueous solution during the early Martian alteration was mainly basic or acidic.

In this context, analcime can be recorded as a mineralogical marker that constrained the coupled aqueous–geological history of Mars. On Earth, hydrothermal environments containing primitive bacteria are thought to correspond to the expected location of the origin of life [92–94]. Similarly, the evidence of hydrothermal phenomena on Martian rocks could be an indication of the development of a biochemical system as a precursor of life.

Author Contributions: A.B. conceived the research and performed XRPD, DSC/TG, TEM measurements, and experimental runs; he analyzed the results and wrote the manuscript; C.B.C. performed the observation under the binocular microscope, SEM observations, analyses and TEM observations of the volcanic ash, analyzed the results and wrote the manuscript; R.D.R. reviewed the manuscript. All authors have read and agreed to the published version of the manuscript.

Funding: This research received no external funding.

Acknowledgments: The authors greatly thank Mariano Davoli from the University of Calabria for his assistance during SEM and microprobe analyses and Giancarlo Niceforo from the University of Calabria for XRF and XRPD analyses. The authors also wish to thank the three competent referees for their work that certainly improved the quality of the manuscript.

Conflicts of Interest: The authors declare no conflict of interest.

References

1. Poulet, F.; Bibring, J.-P.; Mustard, J.F.; Gendrin, A.; Mangold, N.; Langevin, Y.; Arvidson, R.E.; Gondet, B.; Gomez, C. Phyllosilicates on Mars and implications for early Martian climate. *Nature* **2005**, *438*, 623–627. [CrossRef] [PubMed]
2. Gendrin, A.; Mangold, N.; Bibring, J.-P.; Langevin, Y.; Gondet, B.; Poulet, F.; Bonello, G.; Quantin, C.; Mustard, J.; Arvidson, R.; et al. Sulfates in Martian layered terrains: The OMEGA/Mars Express view. *Science* **2005**, *307*, 1587–1591. [CrossRef] [PubMed]
3. Bibring, J.-P.; Langevin, Y.; Mustard, J.F.; Poulet, F.; Arvidson, R.; Gendrin, A.; Gondet, B.; Mangold, N.; Pinet, P.; Forget, F. Global mineralogical and aqueous Mars history derived from OMEGA/Mars Express data. *Science* **2006**, *312*, 400–404. [CrossRef] [PubMed]
4. Mustard, J.F.; Murchie, S.L.; Pelkey, S.M.; Ehlmann, B.L.; Milliken, R.E.; Grant, J.A.; Bibring, J.-P.; Poulet, F.; Bishop, J.; Dobrea, E.N.; et al. Hydrated silicate minerals on Mars observed by the CRISM instrument on MRO. *Nature* **2008**, *454*, 305–309. [CrossRef] [PubMed]
5. Ehlmann, B.L.; Berger, G.; Mangold, N.; Michalski, J.R.; Catling, D.C.; Ruff, S.W.; Chassefière, E.; Niles, P.B.; Chevrier, V.; Poulet, F. Geochemical Consequences of Widespread Clay Mineral Formation in Mars' Ancient Crust. *Space Sci. Rev.* **2013**, *174*, 329–364. [CrossRef]
6. Ming, D.W.; Gooding, J.L. Zeolites on Mars: Possible environmental indicators in soils and sediments. In *Workshop on Mars Sample Return Science, Proceedings of A Lunar and Planetary Institute Workshop, Houston, TX, USA, 16–18 November 1987*; Drake, M.J., Greeley, R., McKay, G.A., Blanchard, D.P., Carr, M.H., Gooding, J., McKay, C.P., Spudis, P.D., Squyres, S.W., Eds.; Lunar and Planetary Institute: Houston, TX, USA, 1988; pp. 124–125.

7. Ehlmann, B.L.; Mustard, J.F.; Murchie, S.L.; Bibring, J.P.; Meunier, A.; Fraeman, A.A.; Langevin, Y. Subsurface water and clay mineral formation during the early history of Mars. *Nature* **2011**, *479*, 53–60. [CrossRef] [PubMed]
8. Viviano, C.E.; Moersch, J.E.; McSween, H.Y. Implications for early hydrothermal environments on Mars through the spectral evidence for carbonation and chloritization reactions in the Nili Fossae region. *J. Geophys. Res. Planets* **2013**, *118*, 1858–1872. [CrossRef]
9. Viviano-Beck, C.E.; Murchie, S.L.; Beck, A.W.; Dohm, J.M. Compositional and structural constraints on the geologic history of eastern Tharsis rise, Mars. *Icarus* **2017**, *284*, 43–58. [CrossRef]
10. Wray, J.J.; Murchie, S.L.; Squyres, S.W.; Seelos, F.P.; Tornabene, L.L. Diverse aqueous environments on ancient Mars revealed in the southern highlands. *Geology* **2009**, *37*, 1043–1046. [CrossRef]
11. Ansan, V.; Loizeau, D.; Mangold, N.; Le Mouélic, S.; Carter, J.; Poulet, F.; Dromart, G.; Lucas, A.; Bibring, P.; Gendrin, A.; et al. Stratigraphy, mineralogy, and origin of layered deposits inside Terby crater, Mars. *Icarus* **2011**, *211*, 273–304. [CrossRef]
12. Carter, J.; Loizeau, D.; Mangold, N.; Poulet, F.; Bibring, J.-P. Widespread surface weathering on early Mars: A case for a warmer and wetter climate. *Icarus* **2015**, *248*, 373–382. [CrossRef]
13. Carter, J.; Poulet, F.; Bibring, J.; Murchie, S.; Ansan, V.; Mangold, N. Mineralogy of layered deposits in Terby Crater, N. Hellas Planitia. In Proceedings of the 41st Lunar and Planetary Science Conference, The Woodlands, TX, USA, 1–5 March 2010.
14. Carter, J.; Poulet, F.; Bibring, J.P.; Mangold, N.; Murchie, S. Hydrous minerals on Mars as seen by the CRISM and OMEGA imaging spectrometers: Updated global view. *J. Geophys. Res. Planets* **2013**, *118*, 831–858. [CrossRef]
15. Pajola, M.; Rossato, S.; Carter, J.; Baratti, E.; Pozzobon, R.; Erculiani, M.S.; Coradini, M.; McBride, K. Eridania Basin: An ancient paleolake floor as the next landing site for the Mars 2020 rover. *Icarus* **2016**, *275*, 163–182. [CrossRef]
16. Singer, R.; McCord, T.; Clark, R.; Adams, J.; Huguenin, R. Mars surface composition from reflectance spectroscopy: A summary. *J. Geophys. Res.* **1979**, *84*, 8415–8426. [CrossRef]
17. Bell, J.F.; McCord, T.B.; Owensby, P.D. Observational evidence of crystalline iron oxides on Mars. *J. Geophys. Res.* **1990**, *95*, 14447–14461. [CrossRef]
18. Ehlmann, B.L.; Mustard, J.F.; Clark, R.N.; Swayze, G.A.; Murchie, S.L. Evidence for low-grade metamorphism, hydrothermal alteration, and diagnosis on Mars from phyllosilicate mineral assemblages. *Clays Clay Miner.* **2011**, *59*, 359–377. [CrossRef]
19. Gooding, J.L. Soil mineralogy and chemistry on Mars: Possible clues from salts and clays in SNC meteorites. *Icarus* **1992**, *99*, 28–41. [CrossRef]
20. Treiman, A.H.; Barrett, R.A.; Gooding, J.L. Preterrestrial aqueous alteration of the Lafayette (SNC) meteorite. *Meteoritics* **1993**, *28*, 86–97. [CrossRef]
21. Sharp, Z.; Williams, J.; Shearer, C.; Agee, C.; McKeegan, K. The chlorine isotope composition of Martian meteorites 2. Implications for the early solar system and the formation of Mars. *Meteorit. Planet. Sci.* **2016**, *51*, 2111–2126. [CrossRef]
22. Chevrier, V.; Mathé, P.E. Mineralogy and evolution of the surface of Mars: A review. *Planet. Space Sci.* **2007**, *55*, 289–314. [CrossRef]
23. Berger, G.; Toplis, M.J.; Treguier, E.; d'Uston, C.; Pinet, P. Evidence in favor of small amounts of ephemeral and transient water during alteration at Meridiani Planum, Mars. *Am. Mineral.* **2009**, *94*, 1279–1282. [CrossRef]
24. Poulet, F.; Gomez, C.; Bibring, J.-P.; Langevin, Y.; Gondet, B.; Pinet, P.; Belluci, G.; Mustard, J. Martian surface mineralogy from Observatoire pour la Mine'ralogie, l'Eau, les Glaces et l'Activite' on board the Mars Express spacecraft (OMEGA/MEx): Global mineral maps. *J. Geophys. Res.* **2007**, *112*, 08S02. [CrossRef]
25. Ehlmann, B.L.; Mustard, J.F.; Swayze, G.A.; Clark, R.N.; Bishop, J.L.; Poulet, F.; Des Marais, D.J.; Roach, L.H.; Milliken, R.E.; Wray, J.J.; et al. Identification of hydrated silicate minerals on Mars using MRO-CRISM: Geologic context near Nili Fossae and implications for aqueous alteration. *J. Geophys. Res.* **2009**, *114*, 1–33. [CrossRef]
26. Yokomori, Y.; Idaka, S. The crystal structure of analcime. *Microporous Mesoporous Mater.* **1998**, *21*, 365–370. [CrossRef]
27. Ferraris, G.; Jones, D.W.; Terkess, J. A neutron-diffraction study of the crystal structure of analcime, $NaAlSi_2O_6 \cdot H_2O$. *Z. Krist. Cryst. Mater.* **1972**, *135*, 240–252. [CrossRef]
28. Ballirano, P.; Pacella, A.; Bloise, A.; Giordani, M.; Mattioli, M. Thermal Stability of Woolly Erionite-K and Considerations about the Heat-Induced Behaviour of the Erionite Group. *Minerals* **2018**, *8*, 28. [CrossRef]

29. Ballirano, P.; Bloise, A.; Gualtieri, A.F.; Lezzerini, M.; Pacella, A.; Perchiazzi, N.; Dogan, M.; Dogan, A.U. The crystal structure of mineral fibers. In *Mineral Fibers: Crystal Chemistry, Chemical-Physical Properties, Biological Interaction and Toxicity*; Gualtieri, A.F., Ed.; European Mineralogical Union: London, UK, 2017; Volume 18, pp. 17–53.
30. Bandfield, J.L.; Hamilton, V.E.; Christensen, P.R. A global view of martian surface compositions from MGS-TES. *Science* **2000**, *287*, 1626–1630. [CrossRef]
31. Hoefen, T.M.; Clark, R.N.; Bandfield, J.L.; Smith, M.D.; Pearl, J.C.; Christensen, P.R. Discovery of olivine in the Nili Fossae region of Mars. *Science* **2003**, *302*, 627–630. [CrossRef]
32. Mustard, J.F.; Poulet, F.; Gendrin, A.; Bibring, J.-P.; Langevin, Y.; Gondet, B.; Mangold, N.; Bellucci, G.; Altieri, F. Olivine and pyroxene diversity in the crust of Mars. *Science* **2005**, *307*, 1594–1597. [CrossRef]
33. Hamilton, V.E.; Christensen, P.R. Evidence for extensive, olivine-rich bedrock on Mars. *Geology* **2005**, *33*, 433–436. [CrossRef]
34. Hamilton, V.E.; Christensen, P.R.; McSween, H.Y., Jr.; Bandfield, J.L. Searching for the source regions of Martian meteorites using MGS TES: Integrating Martian meteorities into the global distribution of igneous materials on Mars, Meteorit. *Planet. Sci.* **2003**, *38*, 871–885.
35. Allen, C.C.; Gooding, J.L.; Keil, K. Hydrothermally altered impact melt rock and breccia: Contributions to the soil of Mars. *J. Geophys. Res. Solid Earth.* **1982**, *87*, 10083–10101. [CrossRef]
36. Naumov, M.V. Principal features of impact-generated hydrothermal circulation systems: Mineralogical and geochemical evidence. *Geofluids* **2005**, *5*, 165–184. [CrossRef]
37. Weisenberger, T.; Selbekk, R.S. Multi-stage zeolite facies mineralization in the Hvalfjordur area, Iceland. *Int. J. Earth Sci.* **2008**, *98*, 985–999. [CrossRef]
38. Robert, C.; Goffe, B. Zeolitisation of basalts in subaqueous freshwater settings: Field observations and experimental studies. *Geochim. Cosmochim. Acta* **1993**, *57*, 3597–3612. [CrossRef]
39. Hay, R.L. Geologic occurrence of zeolites and some associated minerals. *Pure Appl. Chem.* **1986**, *58*, 1339–1342. [CrossRef]
40. Eugster, H.P. Geochemistry of evaporitic lacustrine deposits. *Annu. Rev. Earth Planet. Sci.* **1980**, *8*, 35–63. [CrossRef]
41. Sheppard, R.A.; Hay, R.L. Formation of zeolites in open hydrologic systems. *Rev. Mineral. Geochem.* **2001**, *45*, 261–275. [CrossRef]
42. Line, C.M.B.; Putnis, A.; Putnis, C.; Giampaolo, C. The dehydration kinetics and microtexture of analcime from two parageneses. *Am. Mineral.* **1995**, *80*, 268–279. [CrossRef]
43. Luhr, J.F.; Kyser, T.K. Primary igneous analcime: The Colima minettes. *Am. Mineral.* **1989**, *74*, 216–223.
44. Sætre, C.; Hellevang, H.; Riu, L.; Dypvik, H.; Pilorget, C.; Poulet, F.; Werner, S.C. Experimental hydrothermal alteration of basaltic glass with relevance to Mars. *Meteorit. Planet. Sci. 2019 54*, 357–378. [CrossRef]
45. Viennet, J.C.; Bultel, B.; Riu, L.; Werner, S.C. Dioctahedral phyllosilicates versus zeolites and carbonates versus zeolites competitions as constraints to understanding early Mars alteration conditions. *J. Geophys. Res. Planets* **2017**, *122*, 2328–2343. [CrossRef]
46. Hellevang, H.; Dypvik, H.; Kalleson, E.; Pittarello, L.; Koeberl, C. Can alteration experiments on impact melts from El'gygytgyn and volcanic glasses shed new light on the formation of the Martian surface? *Meteorit. Planet. Sci.* **2013**, *48*, 1287–1295. [CrossRef]
47. Gysi, A.P.; Stefánsson, A. CO_2-water–basalt interaction. Low temperature experiments and implications for CO_2 sequestration into basalts. *Geochim. Cosmochim. Acta* **2012**, *81*, 129–152. [CrossRef]
48. De'Gennaro, M.; Langella, A.; Cappelletti, P.; Colella, C. Hydrothermal conversion of trachytic glass to zeolite. 3. Monocationic model glasses. *Clays Clay Miner.* **1999**, *47*, 348–357. [CrossRef]
49. Taddeucci, J.; Pompilio, M.; Scarlato, P. Conduit processes during the July–August 2001 explosive activity of Mt. Etna (Italy): Inferences from glass chemistry and crystal size distribution of ash particles. *J. Volcanol. Geotherm. Res.* **2004**, *137*, 33–54. [CrossRef]
50. Wang, X.; Boselli, A.; D'Avino, L.; Pisani, G.; Spinelli, N.; Amodeo, A.; Perrone, M.R. Volcanic dust characterization by EARLINET during Etna's eruptions in 2001–2002. *Atmos. Environ.* **2008**, *42*, 893–905. [CrossRef]
51. Witter, J.B.; Hamilton, V.E.; Houghton, B.F. Thermal infrared spectroscopy of explosively erupted terrestrial basalts: Potential analogues for surface compositions on Mars. In Proceedings of the 36th Lunar and Planetary Science Conference, League City, TX, USA, 14–18 March 2005.

52. Ákos, K.; Csorba, Á. Ásványok és kőzetek vizsgálata a Mars felszínén: Vizsgálati, meghatározási lehetőségek. *Földtani Közlöny* **2010**, *40/3*, 293–302.
53. McSween, H.Y.; Wyatt, M.B.; Gellert, R.; Bell, J.; Morris, R.V.; Herkenhoff, K.E.; Crumpler, L.S.; Milam, K.A.; Stockstill, K.R.; Tornabene, L.L. Characterization and petrologic interpretation of olivine-rich basalts at Gusev Crater, Mars. *J. Geophys. Res.* **2006**, *111*, 1–17. [CrossRef]
54. Utada, M. Zeolites in hydrothermally altered rocks. *Rev. Mineral. Geochem.* **2001**, *45*, 30–322. [CrossRef]
55. Hurowitz, J.A.; McLennan, S.L. A~3.5 Ga record of water-limited, acidic weathering conditions on Mars. *Earth Planet. Sci. Lett.* **2007**, *260*, 432–443. [CrossRef]
56. Wang, A.; Korotev, R.L.; Jolliff, B.L.; Haskin, L.A.; Crumpler, L.; Farrand, W.H.; Herkenhoff, K.E.; de Souza Jr., P.; Kusack, A.G.; Hurowitz, J.A.; et al. Evidence of phyllosilicates in Wooly Patch, an altered rock encountered at West Spur, Columbia Hills, by the Spirit rover in Gusev crater, Mars. *J. Geophys. Res.* **2006**, *111*, 1–22. [CrossRef]
57. Ayris, P.; Delmelle, P. Volcanic and atmospheric controls on ash iron solubility: A review. *Phys. Chem. Earth* **2012**, *45*, 103–112. [CrossRef]
58. Farquhar, J.; Savarino, J.; Jackson, T.L.; Thiemens, M.H. Evidence of atmospheric sulphur in the martian regolith from sulphur isotopes in meteorites. *Nature* **2000**, *404*, 50–52. [CrossRef]
59. Young, R.A. Introduction to the Rietveld method. In *The Rietveld Method*; Young, R.A., Ed.; Oxford University Press: Oxford, UK, 1993; pp. 1–38.
60. Gualtieri, A.F.; Gatta, G.D.; Arletti, R.; Artioli, G.; Ballirano, P.; Cruciani, G.; Guagliardi, A.; Malferrari, D.; Masciocchi, N.; Scardi, P. Quantitative phase analysis using the Rietveld method: Towards a procedure for checking the reliability and quality of the results. *Period. Mineral.* **2019**, *88*, 147–151.
61. Feng, S.H.; Li, G.H. Hydrothermal and solvothermal syntheses. In *Modern Inorganic Synthetic Chemistry*, 2nd ed.; Xu, R., Xu, Y., Eds.; Elsevier: Amsterdam, The Netherlands, 2017; pp. 73–104.
62. Jing, Z.; Cai, K.; Li, Y.; Fan, J.; Zhang, Y.; Miao, J.; Jin, F. Hydrothermal synthesis of pollucite, analcime and their solid solutions and analysis of their properties. *J. Nucl. Mater.* **2017**, *488*, 63–69. [CrossRef]
63. Walton, R.I. Subcritical solvothermal synthesis of condensed inorganic materials. *Chem. Soc. Rev.* **2002**, *31*, 230–238. [CrossRef]
64. Krammer, P.; Vogel, H. Hydrolysis of esters in subcritical and supercritical water. *J. Supercrit. Fluids* **2000**, *16*, 189–206. [CrossRef]
65. LeBas, M.J.; Lemaitre, R.W.; Streckeisen, A.; Zanettin, B. A chemical classification of volcanic rocks based on total alkali silica diagram. *J. Petrol.* **1986**, *27*, 745–750.
66. Le Maitre, R.W.; Streckeisen, A.; Zanettin, B.; Le Bas, M.; Bonin, B.; Bateman, P. *Igneous Rocks: A Classification and Glossary of Terms: Recommendations of the International Union of Geological Sciences Subcommission on the Systematics of Igneous Rocks*; Cambridge University Press: New York, NY, USA, 2002.
67. Treiman, A.H.; Bish, D.L.; Vaniman, D.T.; Chipera, S.J.; Blake, D.F.; Ming, D.W.; Morris, R.V.; Bristow, T.F.; Morrison, S.M.; Baker, M.B.; et al. Mineralogy, provenance, and diagenesis of a potassic basaltic sandstone on Mars: CheMin X-ray diffraction of the Windjana sample (Kimberley area, Gale Crater). *J. Geophys. Res. Planets.* **2016**, *121*, 75–106. [CrossRef]
68. Filiberto, J.; Chin, E.; Day, J.M.D.; Franchi, I.A.; Greenwood, R.C.; Gross, J.; Penniston-Dorland, S.C.; Schwenzer, S.P.; Treiman, A.H. Geochemistry of intermediate olivine-phyric shergottite Northwest Africa 6234, with similarities to basaltic shergottite Northwest Africa 480 and olivine-phyric shergottite Northwest Africa 2990. *Meteorit. Planet. Sci.* **2012**, *47*, 1256–1273. [CrossRef]
69. Clark, B.C.; Baird, A.K.; Weldon, R.J.; Tsusaki, D.M.; Schnabel, L.; Candelaria, M.P. Chemical composition of Martian fines. *J. Geophys. Res.* **1982**, *87*, 10059–10067. [CrossRef]
70. Christensen, P.R.; Bandfield, J.L.; Smith, M.D.; Hamilton, V.E.; Clark, R.N. Identification of a basaltic component on the martian surface from Thermal Emission Spectrometer data. *J. Geophys. Res.* **2000**, *105*, 9609–9621. [CrossRef]
71. Wyatt, M.B.; McSween, H.Y., Jr. Spectral evidence for weathered basalt as an alternative to andesite in the northern lowlands of Mars. *Nature* **2002**, *417*, 263–266. [CrossRef]
72. Coombs, D.S.; Whetten, T. Composition of analcime from sedimentary and burial metamorphic rocks. *Geol. Soc. Am. Bull.* **1967**, *78*, 269–282. [CrossRef]
73. Sugano, N.; Kyono, A. An experimental study of symmetry lowering of analcime. *Phys. Chem. Miner.* **2018**, *45*, 381–390. [CrossRef]

74. Mumpton, F.A.; Ormsby, W.C. Morphology of zeolites in sedimentary rocks by scanning electron microscopy. *Clays Clay Miner.* **1976**, *24*, 1–23. [CrossRef]
75. Cruciani, G.; Gualtieri, A. Dehydration dynamics of analcime by in situ synchrotron powder diffraction. *Am. Mineral.* **1999**, *84*, 112–119. [CrossRef]
76. Koizumi, M. The differential thermal analysis curves and the dehydration curves of zeolites. *Mineral. J.* **1953**, *1*, 36–47. [CrossRef]
77. Bloise, A.; Kusiorowski, R.; Lassinantti Gualtieri, M.; Gualtieri, A.F. Thermal behaviour of mineral fibers. In *Mineral Fibers: Crystal Chemistry, Chemical-Physical Properties, Biological Interaction and Toxicity*; Gualtier, A.F., Ed.; European Mineralogical Union: London, UK, 2017; Volume 18, pp. 215–252.
78. Cannata, C.B.; De Rosa, R.; Donato, P.; Taddeucci, J. Ash Features from Ordinary Activity at Stromboli Volcano. *Int. J. Geosci.* **2014**, *5*, 1361–1382. [CrossRef]
79. Bloise, A. Synthesis and characterization of gillespite. *Appl. Phys. A* **2018**, *124*, 330. [CrossRef]
80. Berger, G.; Cathala, A.; Fabre, S.; Borisova, A.Y.; Pages, A.; Aigouy, T.; Esvan, J.; Pinet, P. Experimental exploration of volcanic rocks-atmosphere interaction under Venus surface conditions. *Icarus* **2019**, *329*, 8–23. [CrossRef]
81. Berger, G.; Claparols, C.; Guy, C.; Daux, V. Dissolution rate of a basalt glass in silica-rich solutions: Implications for long-term alteration. *Geochim. Cosmochim. Acta* **1994**, *58*, 4875–4886. [CrossRef]
82. Crovisier, J.; Advocat, T.; Dussossoy, J. Nature and role of natural alteration gels formed on the surface of ancient volcanic glasses (Natural analogs of waste containment glasses). *J. Nucl. Mater.* **2003**, *321*, 91–109. [CrossRef]
83. Hellmann, R.; Cotte, S.; Cadel, E.; Malladi, S.; Karlsson, L.S.; Lozano-Perez, S.; Cabie, M.; Seyeux, A. Nanometre- scale evidence for interfacial dissolution-reprecipitation control of silicate glass corrosion. *Nat. Mater.* **2015**, *14*, 307–311. [CrossRef]
84. Michalski, J.; Poulet, F.; Bibring, J.P.; Mangold, N. Analysis of phyllosilicate deposits in the Nili Fossae region of Mars: Comparison of TES and OMEGA data. *Icarus* **2010**, *206*, 269–289. [CrossRef]
85. Hausrath, E.M.; Navarre-Sitchler, A.K.; Sak, P.B.; Steefel, C.I.; Brantley, S.L. Basalt weathering rates on Earth and the duration of liquid water on the plains of Gusev Crater, Mars. *Geology* **2008**, *36*, 67–70. [CrossRef]
86. Carrozzo, F.G.; Di Achille, G.; Salese, F.; Altieri, F.; Bellucci, G. Geology and mineralogy of the Auki Crater, Tyrrhena Terra, Mars: A possible post impact induced hydrothermal system. *Icarus* **2017**, *281*, 228–239. [CrossRef]
87. Rathbun, J.A.; Squyres, S.W. Hydrothermal systems associated with Martian impact craters. *Icarus* **2002**, *157*, 362–372. [CrossRef]
88. Abramov, O.; Kring, D.A. Impact-induced hydrothermal activity on early Mars. *J. Geophys. Res. Planets* **2005**, *110*, E12S09. [CrossRef]
89. Schwenzer, S.P.; Kring D., A. Impact-generated hydrothermal systems capable of forming phyllosilicates on Noachian Mars. *Geology* **2009**, *37*, 1091–1094. [CrossRef]
90. Wang, A.; Haskin, L.A.; Squyres, S.W.; Jolliff, B.L.; Crumpler, L.; Gellert, R.; Schröder, C.; Herkenhoff, K.; Hurowitz, J.; Tosca, N.J.; et al. Sulfate deposition in subsurface regolith in Gusev crater, Mars. *J. Geophys. Res. Planets* **2006**, *111*, 1–19. [CrossRef]
91. Peretyazhko, T.S.; Sutter, B.; Morris, R.V.; Agresti, D.G.; Le, L.; Ming, D.W. Fe/Mg smectite formation under acidic conditions on early Mars. *Geochim. Cosmochim. Acta* **2016**, *173*, 37–49. [CrossRef]
92. Shock, E.L. Hydrothermal systems as environments for the emergence of life. *Ciba Found Symp.* **1996**, *202*, 40–60.
93. Newsom, H.E.; Hagerty, J.J.; Goff, F. Mixed hydrothermal fluids and the origin of the Martian soil. *J. Geophys. Res. Planets.* **1999**, *104*, 8717–8728. [CrossRef]
94. Newsom, H.E.; Hagerty, J.J.; Thorsos, I.E. Location and sampling of aqueous and hydrothermal deposits in Martian impact craters. *Astrobiology* **2001**, *1*, 71–88. [CrossRef]



© 2020 by the authors. Licensee MDPI, Basel, Switzerland. This article is an open access article distributed under the terms and conditions of the Creative Commons Attribution (CC BY) license (http://creativecommons.org/licenses/by/4.0/).